Int. J. Electrochem. Sci., 11 **(2016)** 4092 - 4109

International Journal of
ELECTROCHEMICAL
SCIENCE
www.electrochemsci.org

Three-dimensional Cage-like Co_3O_4 Structure Constructed by Nanowires for Supercapacitor

Yarong Liang, Yuying Yang, Zhongai Hu[*], *Yadi Zhang, Zhimin Li, Ning An, and Hongying Wu*

Key Laboratory of Eco-Environment-Related Polymer Materials of Ministry of Education, Key Laboratory of Polymer Materials of Gansu Province, College of Chemistry and Chemical Engineering, Northwest Normal University, Lanzhou, Gansu 730070, P R China,
[*]E-mail: zhongai@nwnu.edu.cn

Received: 8 February 2016 / *Accepted:* 14 March 2016 / *Published:* 1 April 2016

Three-dimensional (3D) cage-like network architecture is constructed by cobalt oxide nanowires on porous nickel foam (donated as 3D cage-like Co_3O_4/NF) via a mild hydrothermal method. A series of measurements including X-ray diffraction (XRD), fourier transform infrared spectroscopy (FT-IR), field emission scanning electron microscopy (FESEM) and transmission electron microscopy (TEM) are used to characterize the crystal structure, component and morphology of the as-prepared sample. The 3D cage-like hierarchical nanostructure increases utilization of active materials and shortens electrolyte ion transport pathway during the charging/discharging processes, leading to the excellent capacitive properties of the electrode materials. In a three-electrode system, the resultant electrode exhibits higher specific capacitance of 642 F g^{-1} and great rate capability (88% capacity retention at 10 A g^{-1}) in 3 M KOH solution. Importantly, the assembled asymmetric supercapacitor with a potential window of 1.7 V, in which 3D cage-like Co_3O_4/NF and graphene hydrogel (GH) are served as positive and negative electrode respectively, achieves the energy density of 31 Wh kg^{-1} along with power density of 854 W kg^{-1}, indicating a promising potential in the applications of energy storage.

Keywords: Cobalt oxide Nanowires; Cage-like architecture; Energy density; Asymmetric supercapacitors

1. INTRODUCTION

The energy consumption has already become a big problem of our society. The production and storage of clean energies are considered as an effective routine to solve this bottle neck problem. [1-4] Supercapacitors (SCs), which have the superiority of short charging time and good circulation stability as emerging energy storage device, are increasingly attracting attention in new energy fields. [5-8] The metal oxides, especially transition metal oxides, play a vital role in the development of supercapacitors due to high energy density. Among of them, Co_3O_4 is expected to be a pseudocapacitive candidate

doi: 10.20964/110451

owing to its well defined electrochemical redox activity and high value of theoretical specific capacitance (3560 F g^{-1}) [9-11]. Pseudocapacitive behavior in Co_3O_4 material originates from fast redox kinetics and reversible Faradaic reaction occurring on the electrode surface. In order to further enhance capacitive performance of Co_3O_4 electrode material, great efforts are devoted to design, regulation and control of its microstructure, as reported in many references. For instance, Liu et al. [12] synthetized the RGO/Co_3O_4 nanosheets hybrid composite with 94.3 wt% Co_3O_4, delivering a specific capacitance of 331 F g^{-1} at the current density of 5 A g^{-1}. Xiao et al. [13] successfully fabricated enoki mushroom-like Co_3O_4 hierarchitectures, leading to the specific capacitance of 787 F g^{-1} at a current density of 1 A g^{-1}, but it showed relatively low energy density (23 Wh kg^{-1}) in the two-electrode system. Xiao et al. [14] reported the mesoporous Co_3O_4 nanoflake array, exhibiting 450 F g^{-1} at 1 A g^{-1} in 2 M KOH aqueous solution. However, the theoretical values are still much larger than the experimental values in specific capacitance, which is attributed to poor conductivity and low utilization of Co_3O_4. Therefore, it is necessary to overcome these disadvantages through improving microstructure and selecting current collector. The nickel foam (NF) is served as a kind of typical current collector to support metal oxides or other materials, owing to its 3D skeleton structure, and it provide more channels for ions transport in electrochemical processes. The traditional preparation of electrode, due to the addition of a polymer binder and conductive agent, will lead to an extra contact resistance and dead surface, thus hinder the diffusion of electrolyte. Nevertheless, in situ growth of active material on the nickel foam could reduce the internal resistance of the electrode, which is conducive to maintain rapid redox reactions and improve the utilization of active material. Recently, Co_3O_4@Graphene/NF [15], CoO@C/NF [16] and $Ni(OH)_2$/NF [17] composites have been reported, presenting excellent performances.

Inspired by the above facts, in this work, we designed and synthesized a 3D cage-like Co_3O_4 architecture supported by porous nickel foam as binder-free electrode for supercapacitor. This unique structure will display several advantages during charging or discharging processes. In the first place, the cage in the architecture can provide an appropriate interspace for storing electrolyte solutions, resulting in an easy diffusion of reacting ions and good features of power. In the second place, the upstanding nanowires supported on the nickel foam are in the well-dispersing state, implying high utilization of Co_3O_4. Finally, the resultant electrode has low overall electrical resistance due to avoiding secondary processing which additive and binder are usually used. These characters let the novel 3D cage-like structure of Co_3O_4/NF exhibit excellent capacitive performance in terms of specific capacitance (as high as 642 F g^{-1} at 1 A g^{-1}) and good rate capability with capacitance retention of 88%. Importantly, the as-assembled asymmetric supercapacitor delivers energy density of 31 Whkg^{-1} with capacity retention of 83% at current density of 1 A g^{-1} after 1500 cycles.

2. EXPERIMENTAL

2.1 Chemicals

Cobalt nitrate [$Co(NO_3)_2 \cdot 6H_2O$], ammonium fluoride (NH_4F), urea [$CO(NH_2)_2$], potassium hydroxide (KOH), graphite powder, sulfuric acid (98%, H_2SO_4), potassium permanganate ($KMnO_4$),

sodium nitrate ($NaNO_3$), hydrogen peroxide (30%, H_2O_2), hydrochloric acid (37%, HCl), acetone (CH_3COCH_3), absolute ethyl alcohol (C_2H_5OH), and deionized (DI) water were referred to our experiment. Analytical reagents without further purification were used in experimental process.

2.2 Preparation of the 3D cage-like Co_3O_4/NF

The preparation process of 3D cage-like Co_3O_4 nanowires structure on nickel foam was as follows. Briefly, 0.25 mmol $Co(NO_3)_2 \cdot 6H_2O$, 0.5 mmol NH_4F and 1.5 mmol of $CO(NH_2)_2$ were first dissolved in 15 mL deionized water under continuously magnetic stirring to form a homogeneous solution, and then the mixed solution was placed in a Teflon-lined autoclave with a volume of 25 mL. A piece of nickel foam with 1cm×3cm×1mm in size was rinsed with acetone, absolute ethyl alcohol, deionized water in an ultrasonic bath in turn, then was immersed into the above autoclave to undergo the continued reaction for 16 h at 120 °C. The precursor was picked out after cooling down to room temperature naturally, then repeatedly washed with deionized water and followed by vacuum drying at 60 °C for 12 h. Finally, the precursor was calcined at 250 °C for 4 h in the air, obtaining the 3D cage-like Co_3O_4/NF. For comparison, other samples were synthesized by controlling the time or temperature (shown in supplementary information).

2.3 Synthesis of GH

Graphite oxide (GO) was derived from graphite powder (325 mesh) by a modified Hummers method, which possessed good dispersion in monolayered sheets as in previous work. [18-20]

The synthesized procedure of GH is as follows. GO (120 mg) was exfoliated in deionized water (30 mL) with 1 h ultrasonic treatment to form a light-brown dispersion. Then, the solution was hydrothermally underwent 180 °C for 12 h. The autoclave was naturally cooled in room temperature, and then, a black cylinder product was obtained. Finally, the black cylinder monolith was taken out, washed with a large amount of deionized water, and freeze-dried into a hydrogel.

2.4 Characterization

The crystallographic structure of sample was characterized by XRD (D/Max-2400, with Cu Kα radiation operating at 40 kV). The components and elemental analysis of materials were examined by FTIR (Bruker Vector-22 FTIR spectrometer at room temperature) and Energy Dispersive X-ray Spectroscopy (EDS). The morphology of the products was studies by FESEM (ULTRA plus, Germany) and TEM (JEOL, JEM-2010, Japan).The specific surface areas and pore-size distributions were tested by N_2 adsorption and desorption experiment at -196 °C using a Micrometrics ASAP 2010 instrument.

2.5 Electrochemical characterization

The electrochemical capacitive performance of individual working electrode were measured on a typical three-electrode system, in which 3D cage-like Co_3O_4/NF directly acted as the working electrode without secondary processing, a platinum foil served as the counter electrode, and a Hg/HgO electrode used as the reference electrode. In order to show the potential in applications, the asymmetric capacitor was assembled, where GH, 3D cage-like Co_3O_4/NF and poly vinyl alcohol (PVA) membrane were served as negative electrode, positive electrode and separator, respectively. As for the GH electrode, the nickel foam is still used as current collector. A slurry containing 85wt% as-prepared GH powders, 10 wt% acetylene black and 5 wt% polytetrafluoroethylene (PTFE) was coated on the nickel foam to fabricate the working electrodes, following by dry at 70 °C for 12 h. All of the above electrochemical experiments were measured by using an electrochemical working station (CHI760E, shanghai, China) in 3 M KOH aqueous solution at room temperature. The cycle stability tests were performed on a LAND battery program-control test system.

The specific capacitance of 3D cage-like Co_3O_4/NF electrode in the three-electrode configuration is calculated from galvanostatic discharge curves using the following equation: [21]

$$C = I \cdot t / m \cdot \Delta V \quad (1)$$

Where C (F g^{-1}) represents the specific capacitance of electrodes, t (s) shows the discharge time, I (A g^{-1}) is current density, ΔV (V) is the potential change during discharging and m (g) is the mass loading on electrodes.

To set up the asymmetric supercapacitor, the optimal mass ratio between the positive and the negative electrode in the two-electrode configuration is expressed as: [22]

$$\frac{m_+}{m_-} = \frac{C_- \cdot \Delta V_-}{C_+ \cdot \Delta V_+} \quad (2)$$

Where C_- and C_+ are the specific capacitance values, ΔV_- and ΔV_+ are the potential window for the charge/discharge process of the negative and positive electrodes, m_+ and m_- are the mass, respectively.

The specific capacitance (C, F g^{-1}), power density (P, W kg^{-1}) and energy density (E, Wh kg^{-1}) of the asymmetric supercapacitor were calculated using the following formulas: [23,24]

$$E = C \cdot \Delta V^2 / 2 \quad (3)$$

$$P = 3600E / t \quad (4)$$

where C is the device capacitance (F g^{-1}) in the two-electrode configuration. While the power density values (P) are obtained by dividing the E with time t for one complete discharging segment.

3. RESULT AND DISCUSSION

3.1 Characterization of Positive electrode

The fabrication process of the 3D cage-like Co_3O_4/NF is presented in Scheme 1. The growth mechanism of 3D cage-like Co_3O_4 network structure on nickel foam is probably explained by "oriented attachment" and "self-assembly" as demonstrated in the previous literature. [25] In the beginning stage of reactions, the hydrolysis of urea gradually release hydroxyl ions (OH^-), leading to

the random formation of $Co(OH)_2$ nucleation on the surface of nickel foam. Reacting still further ahead, $Co(OH)_2$ nanoparticles will form in the vicinity of the resultant nucleation. And then the formed nanoparticles would spontaneously "land" on the as-formed nucleation and gradually grow as an upstanding nanowire through self-assembly. The further oriented attachment of $Co(OH)_2$ nanoparticles is favorable for the longitudinal growth of the nanowires. It needs to note that one end of the formed nanowires is fixed on the surface of nickel foam but the other end is in the footloose state. When the longitudinal length of nanowires is long enough, the non-fixed end of the nanowires is inclined to aggregate into a bundle to decrease the free energy of the system. Finally, these nanowires interweave into a 3D cage-like network architecture.

The relative chemical reactions can be elucidated as: [26]

$$NH_2CONH_2 \xrightarrow{\text{hydrolysis}} NH_4^+ + NCO^- \quad (5)$$

$$NCO^- + 3H_2O \rightarrow HCO_3^- + NH_4^+ + OH^- \quad (6)$$

$$Co^{2+} + 2OH^- \rightarrow Co(OH)_2 \quad (7)$$

$$6Co(OH)_2 + O_2 \rightarrow 2Co_3O_4 + 6H_2O \quad (8)$$

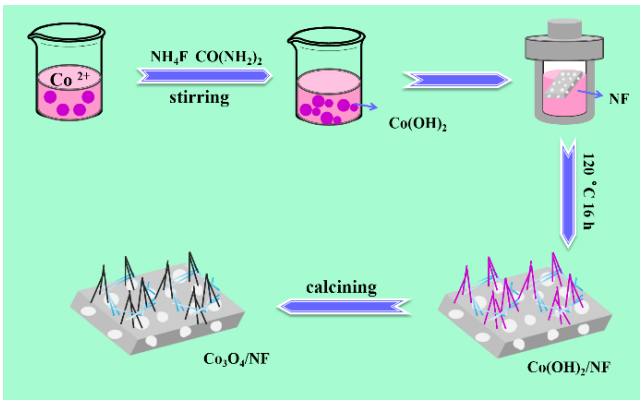

Scheme 1. The formation process of the3D cage-like Co_3O_4/NF.

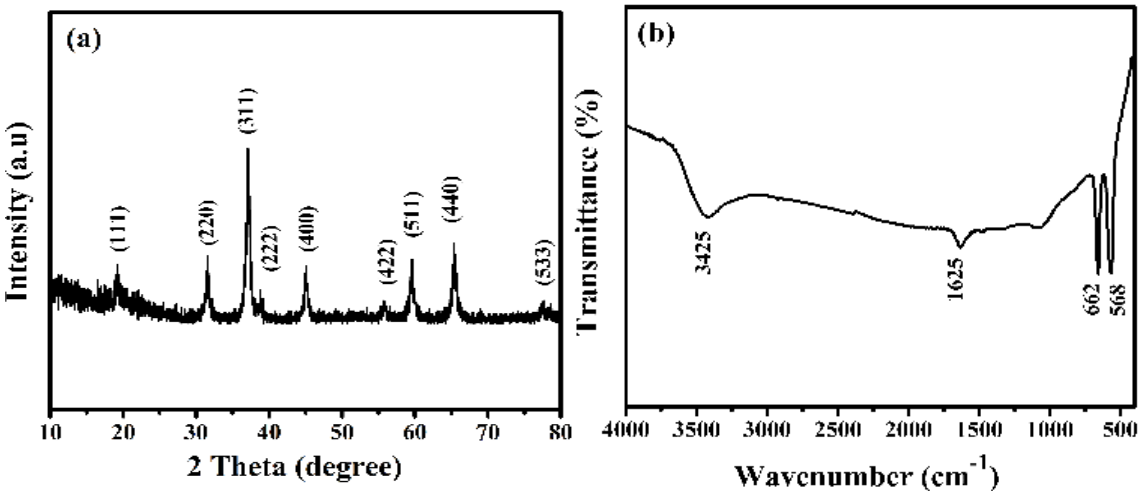

Figure 1. (a) X-ray diffraction patterns, (b) FTIR spectrum of Co_3O_4.

The obtained cage-like Co_3O_4 nanowires is characterized by XRD (Figure 1a). Obviously, the diffraction peaks of Co_3O_4 are observed at the 2θ of 18.9, 31.2, 36.7, 38.5, 44.8, 55.9, 59.3, 65.2 and 77.5°, which could be indexed to the (111), (220), (311), (222), (400), (422), (511), (440) and (533) planes of the cubic spinel Co_3O_4 (JCPDS card No. 42-1467) [27]. The above result confirms the sample deposited after thermal decomposition of the precursors at 250 °C is consisted of Co_3O_4 without impurity phase.

The infrared spectrum of Co_3O_4 is shown in Figure 1b. It shows the typical feature of Co_3O_4. The sharp peaks at 662 and 568 cm^{-1} are assigned to the stretching vibration absorption of Co-O group in spinel cobalt oxide. [28] The peaks around 3425 and 1625 cm^{-1} are due to the surface of the nanocrystals absorbed water molecules and hydroxyls. [29]

The specific surface area and pore size distributions of the as-obtained Co_3O_4 nanowires were investigated by Brunauer-Emmett-Teller (BET) gas-sorption measurements. Figure 2 presents N_2 adsorption and desorption isotherms for the Co_3O_4. The isotherm is regarded as a type III with a hysteresis loop of type H3 in the relative pressure range of 0.5-0.95. The BET specific surface area of the Co_3O_4 was estimated to be 68 m^2 g^{-1}. Moreover, the inset image indicates that the majority of pores are in the mesoporous region with a pore size centered at 8 nm. For the comparison, the specific surface area for various micro- and nano-structured Co_3O_4 materials is shown in Table 1.

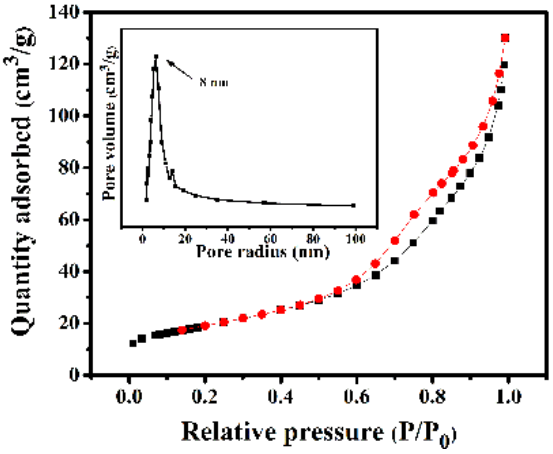

Figure 2. N_2 absorption-desorption isotherm (inset is pore size distribution) for Co_3O_4.

Table 1. the specific surface area for various micro- and nano-structured Co_3O_4 materials.

Micro-structures	Specific surface area	Ref.
Cage-like Co_3O_4	68 m^2 g^{-1}	our work
2D Co_3O_4 thin sheet	54.25 m^2 g^{-1}	[30]
Hollow Co_3O_4 nanoboxes	31.07 m^2 g^{-1}	[31]
Co_3O_4 nanoflakes	97 m^2 g^{-1}	[32]

Figure 3a presents the morphologies of the pure nickel foam. It can be clearly observed that pure nickel foam possesses large pores and smooth surface to provide the firm scaffold for growth of

Co_3O_4 and also serves as conductive current collector for electron transport. [33,34] Figure 3b shows the whole morphology of the as-obtained 3D cage-like Co_3O_4/NF electrode. It can be seen that the surface of nickel foam is covered with the deposited matter. Observed at high magnification (Figure 3c, 3d),the cross-linked Co_3O_4 nanowires distribute throughout nickel foam skeletons homogeneously, meanwhile, forming a loose cage-like structure with pores of 1-2 μm and displaying a novel morphology compared to the previous reports on Co_3O_4. [35,36] This unique structure can not only supply sufficient electrochemical active sites on the surface of Co_3O_4, but increase the effective liquid-solid interfacial area, provide a fast path for the insertion and extraction of electrolyte ions and consequently enhance excellent superior pseudocapacitive performance. In addition, the energy dispersive spectroscopy data proves that cobalt, oxygen and nickel elements exist in the samples as shown in Figure 3e.

In order to further analyze the morphology features of Co_3O_4, TEM was employed in our study. As shown in Figure 3f, the Co_3O_4 nanowire is consisted of numerous nanoparticles, which accumulate with each other to form a polycrystalline structure. Additionally, as displayed in Figure 3g, the distinct fringe spacing is determined to be around 0.24 nm which corresponds to the crystal plane (311) distance of Co_3O_4. The result is consistent with XRD test.

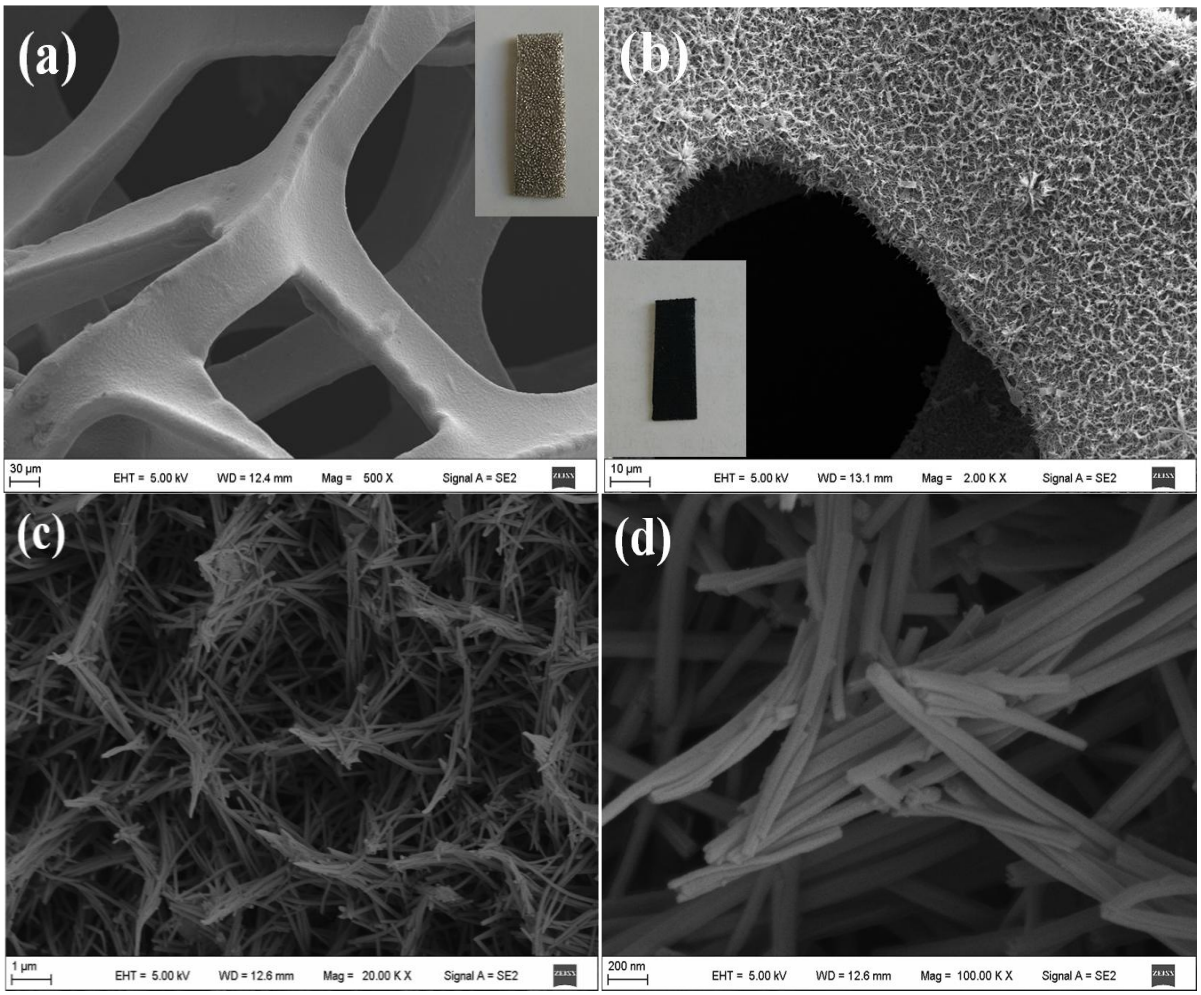

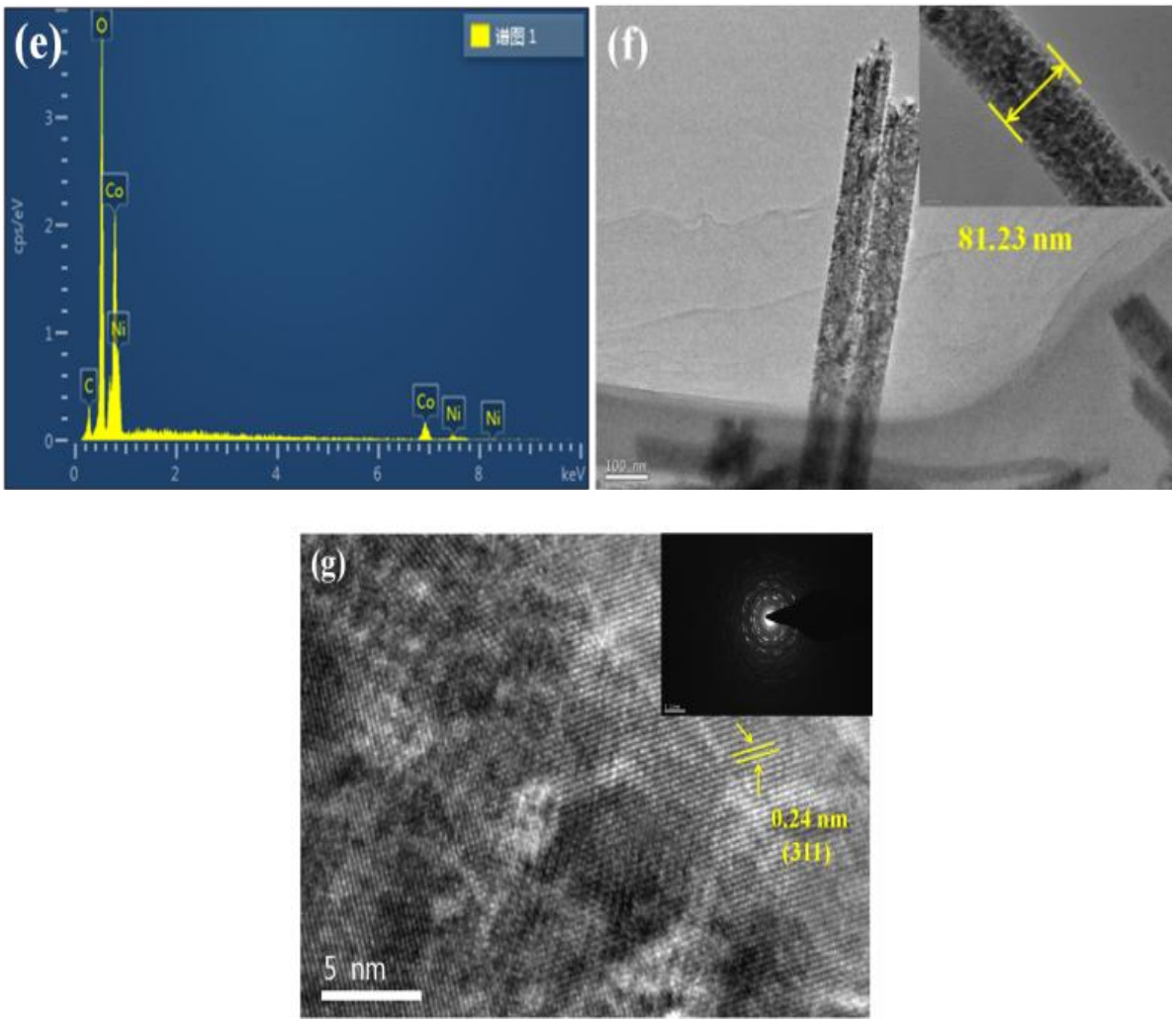

Figure 3. FESEM image of (a) pure nickel foam. (b-d) Low-resolution and high-resolution, (e) EDS spectrum of 3D cage-like Co_3O_4/NF. (f-g) low and high magnification TEM images (Inset in (g) the corresponding SAED pattern) of 3D cage-like Co_3O_4/NF.

The inset in Figure 3g, the selected-area electron diffraction (SAED) pattern, shows a set of well-defined concentric rings, demonstrating the polycrystalline structures of the synthesized sample as well. The diffraction rings can be indexed to the lattice planes as expected from Co_3O_4 with cubic spinel structure.

3.2 Electrochemical tests

Cyclic voltammetry (CV), galvanostatic charge-discharge (GCD) and electrochemical impedance spectroscopy (EIS) are used to characterize the electrochemical performance of 3D cage-like Co_3O_4/NF electrode. They are very prominent to estimate capacitor materials. [37,38] Figure 4a presents the CV curve of the 3D cage-like Co_3O_4/NF electrode at different scan rates within the potential window of 0-0.6 V. A pair of obvious redox peaks can be observed in the CV curves, which

indicate a typical pseudocapacitive behavior from Faradaic redox reaction. The Faradaic reactions can be represented as following reaction: [39]

$$Co_3O_4 + 4OH^- \Leftrightarrow 3CoO_2 + 4e^- + 2H_2O \quad (9)$$

The anodic peak is due to the oxidation of Co_3O_4 to CoO_2 while the cathodic peak is for the reverse process. A small positive shift of the oxidation peak potential and a negative shift of the reduction peak potential have been observed with increased scan rate, which can be primarily attributed to the influence of the increasing electrochemical polarization as the scan rate scales up.

Figure 4b shows the GCD curve of the 3D cage-like Co_3O_4/NF electrode at different current densities. The specific capacitance calculated by the discharge curves are 642, 622, 611, 573 and 564 F g^{-1} at the various current densities of 1, 2, 3, 7 and 10 A g^{-1}, respectively. As the increase of current density, the specific capacitance gradually decreases due to an incomplete accessibility of electrochemically active materials to ions, resulting the low utilization rate of active materials. [40] The specific capacitance can be remained at 88% when the current density increase from 1 to 10 A g^{-1}, which shows excellent rate capability (Figure 4c). In addition, the comparison with literatures is shown Table 2.

Table 2 Supercapacitive comparison between the Co_3O_4/NF in our work and the Co_3O_4 electrode materials reported in other previous literature.

Micro-structures	Current density	Specific capacitance	Ref.
Cage-like Co_3O_4 /NF	2A g^{-1}	622 F g^{-1}	in our work
$Co_3O_4$and Co_3O_4/CoO nanoparticles	4 A g^{-1}	286 F g^{-1}	[4]
CNT@Co_3O_4/NF	1 A g^{-1}	559 F g^{-1}	[41]
Co_3O_4 flim	2A g^{-1}	325 F g^{-1}	[42]
Co_3O_4 nanoflake array film	2A g^{-1}	351 F g^{-1}	[43]
Ultralayered Co_3O_4 nanoflakes	8 A g^{-1}	548 F g^{-1}	[32]

Figure 4d reveals the Nyquist plots with the frequency ranged from 0.1 Hz to 100 kHz for 3D cage-like Co_3O_4/NF electrode. In the high frequency region, there is an obvious semicircle observed. It is associated with the charge-transfer resistance of the electrodes. [44] In addition, the intercept on the real axis stands for the equivalent series resistance. In the low frequency range, the Nyquist plot gives a nearly close to vertical line along the imaginary axis. The low equivalent series resistance and slight electrochemical polarization are relevant to the novel structure. Figure 4e shows the cyclic performance of the 3D cage-like Co_3O_4/NF examined by GCD tests at 2 A g^{-1} for 1500 cycles. As seen from Figure 4e, at the beginning of the test specific capacitance increased gradually, which may be attributed to an activation process in the electrode. [45] The capacitance of 3D cage-like Co_3O_4/NF decrease only 11% after 1500 cycles.

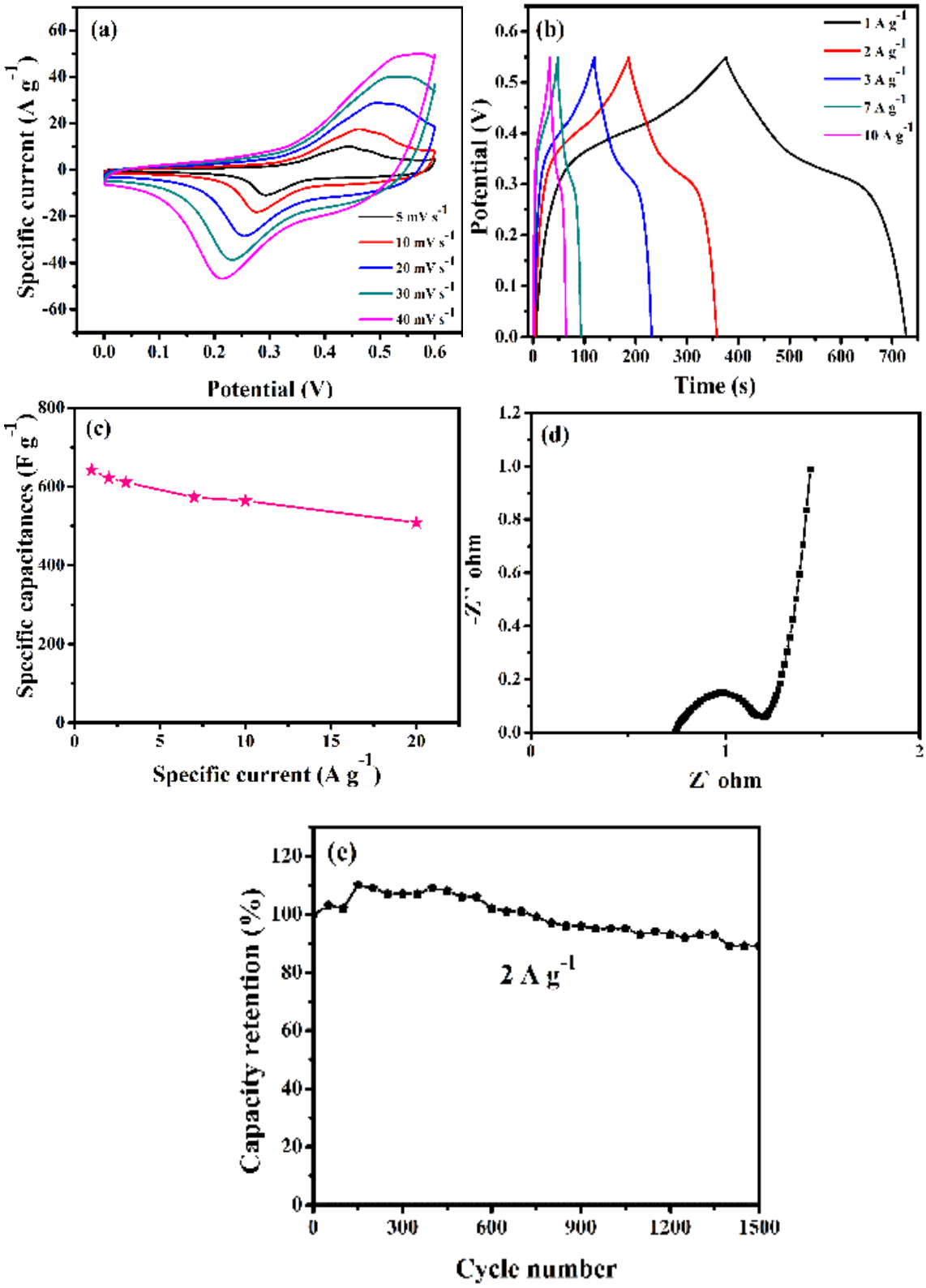

Figure 4. (a) Cyclic voltammograms at different scan rates, (b) Charge-discharge curves at different current densities, (c) Specific capacitances at various discharge current densities, (d) Nyquist plots, (e) Cycling stability and (f) the SEM image of the 3D cage-like Co_3O_4/NF electrode after 1500 cycles.

3.3 Electrochemical tests of Negative electrode

The SEM image of GH is shown in supplementary information (Figure S3). The graphene oxide sheets overlap each other in 3D space to form the interconnected porous network structure.

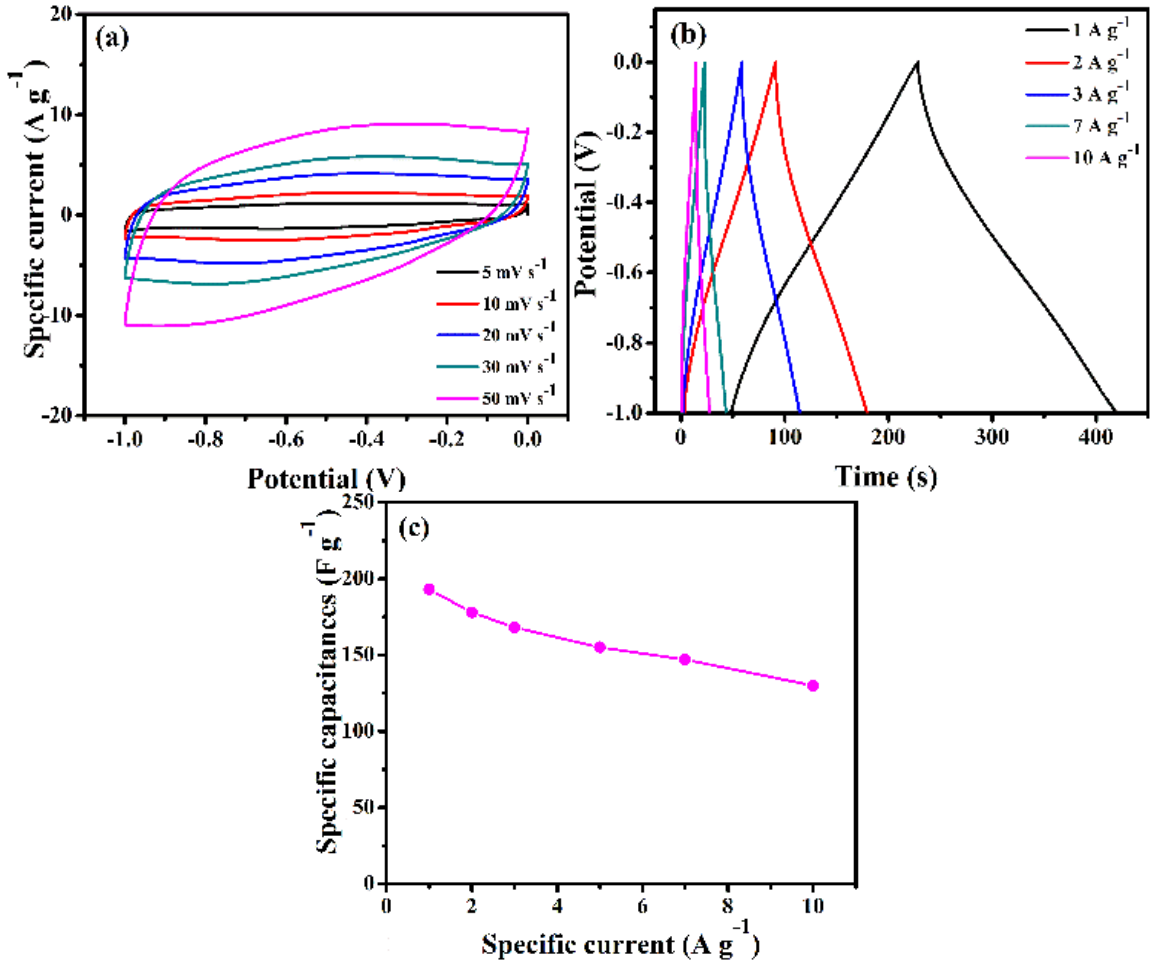

Figure 5. (a) Cyclic voltammogramsat various scan rates. (b) Charge-discharge curves under different current density. (c) Average specific capacitance at various discharge current densities of the GH electrode.

The electrochemical properties of the GH electrode was investigated by using a conventional three-electrode system with Hg/HgO as the reference electrode and platinum plate as the counter electrode in 3 M KOH electrolyte. The CV curves of the GH electrode measured in the potential window of -1.0 V-0 V exhibit nearly rectangular-like shapes (Figure 5a) even at higher scan rate. And the GCD curves of GH electrode are highly linear and symmetrical at various current densities from 1 to 10 A g^{-1} (Figure 5b), which are obvious the characteristics of double layer supercapacitors. Moreover, the capacity values are calculated to be 194, 180, 168, 147 and 130 F g^{-1} at the current density of 1, 2, 3, 7 and 10 A g^{-1}, respectively.

3.4 Asymmetric supercapacitor

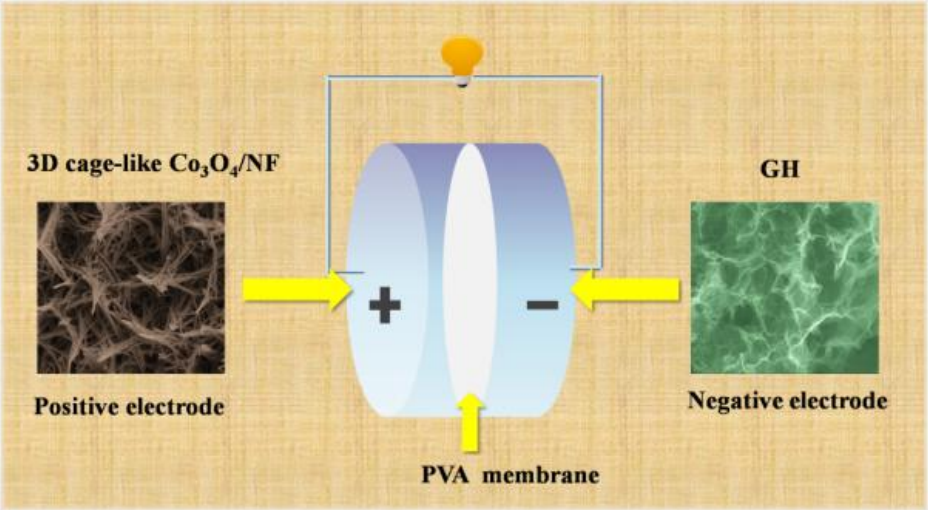

Figure 6. Schematic illustration of the asymmetric supercapacitor device.

By using the 3D cage-like Co_3O_4/NF as a positive electrode and GH as a negative electrode, we constructed a two-electrode system or so-called asymmetric supercapacitor with 3 M KOH aqueous as electrolyte (Figure 6). The electrochemical performances of the as-prepared asymmetric capacitor were investigated by CV and GCD.

Figure 7a depicts the CV curve of GH electrode in the potential window of -1.0 to 0 V, it exhibits a nearly ideal rectangular shape without detectable redox peaks, demonstrating a typical characteristic of electric double layer. While the CV shape of the 3D cage-like Co_3O_4/NF electrode in the potential range of 0-0.6 V, illustrating that the capacitance derives from the contribution of the pseudocapacitance of Co_3O_4. In addition, the lower-limit potential of GH electrode and the upper-limit potential of 3D cage-like Co_3O_4/NF electrode can basically reach -1.0 V and 0.6 V respectively without obvious polarizations, and thus the theoretical maximum potential window of the asymmetric capacitor can reach 1.6 V. Here, the practical potential window could be increased to 1.7 V in order to achieve better electrochemical properties (Figure 7b), which is almost the twice of the conventional metal oxide-based symmetric capacitors in aqueous solution electrolyte.

In an asymmetric capacitor, for getting the charge balance between the two electrodes according to equation (2), the mass ratio of the 3D cage-like Co_3O_4/NF to GH was selected to be 0.55:1. Figure 7e shows the typical GCD curves of the asymmetric capacitor measured at 1 A g^{-1}. The specific capacitances are 78, 71, 65, 59, 49 and 35 F g^{-1} at various current densities of 1, 2, 3, 5, 7 and 10 A g^{-1}, respectively. Its electrochemical capacitive performance can be attributed to the combined contribution of the main redox pseudocapacitance of Co_3O_4 and partly from the electric double layer capacitance of GH. Accordingly, it maintains an energy density of 31 Wh kg^{-1} with power density as high as 854 W kg^{-1} at operating voltages of 1.7 V, which are calculated by equation (3-4). As shown in Figure 7g, the asymmetric supercapacitor delivers a prominent energy density of 31 Wh kg^{-1} at a power density of 854 W kg^{-1}. Moreover, it also can operate at a high power density of 6000 W kg^{-1} with an energy density of 20 Wh kg^{-1}.

As seen from Figure 7f, the intercept on the real axis in the high-frequency range manifest equivalent series resistance. It is noted that the small semicircle is an indication of lower charge-transfer resistance.

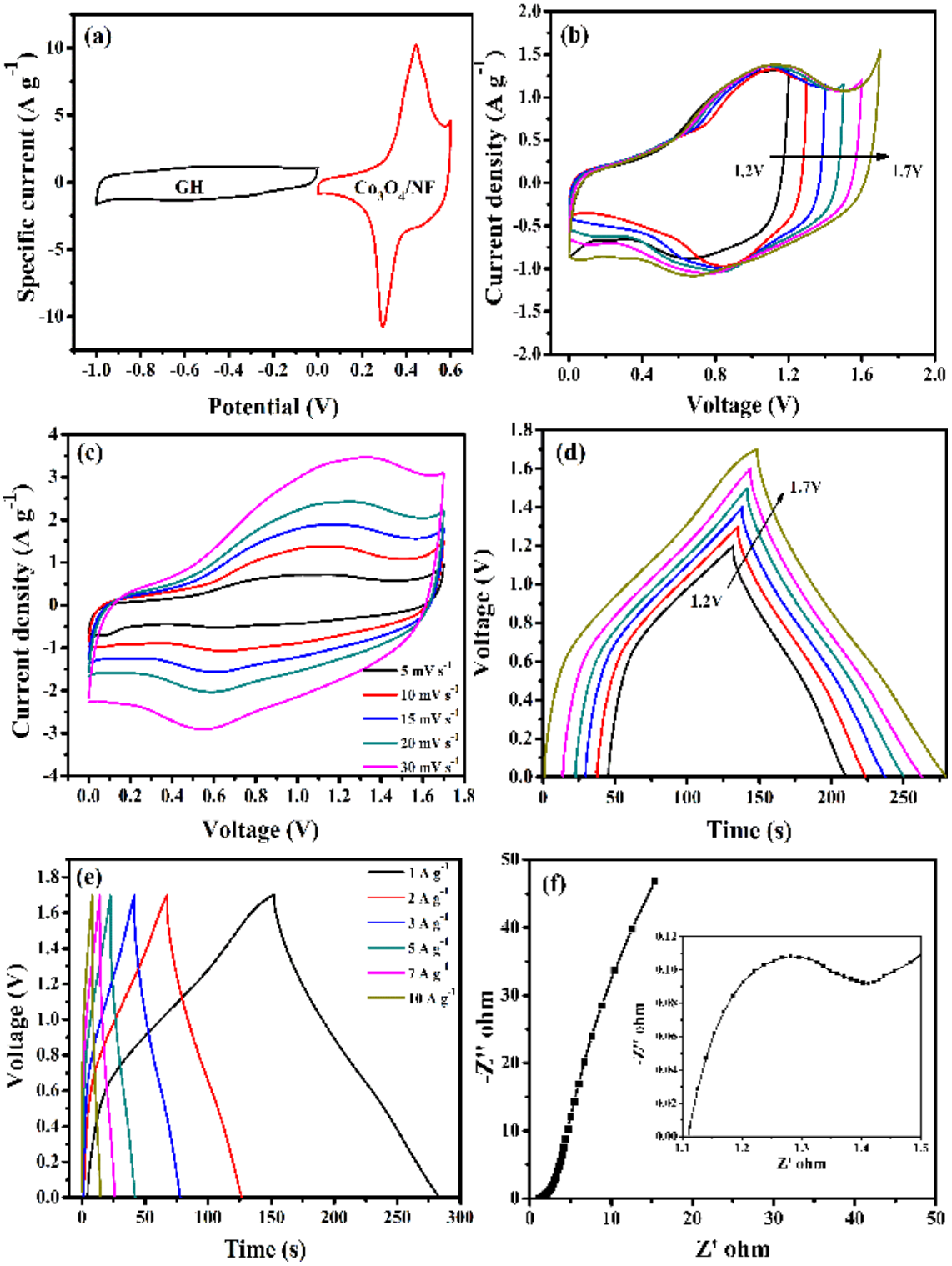

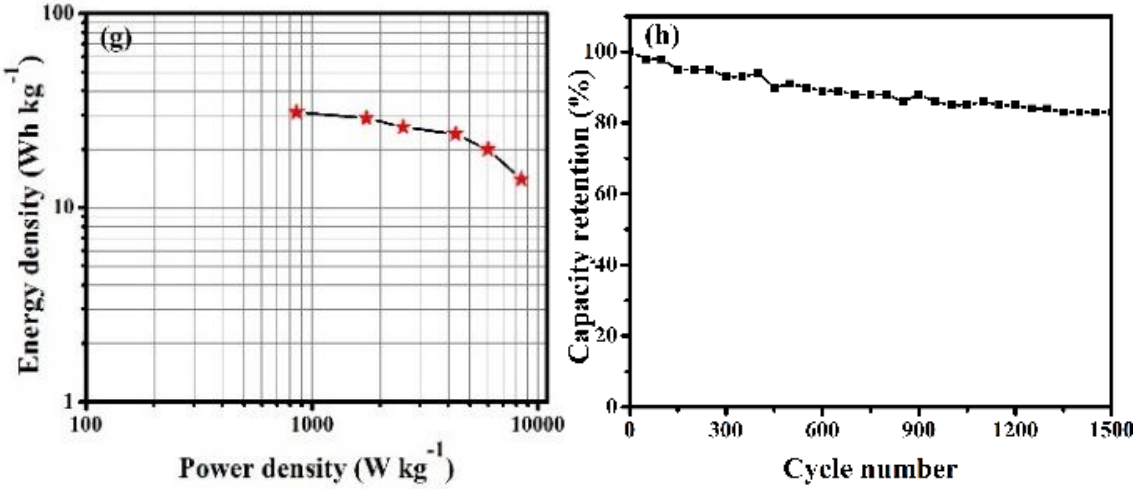

Figure 7. (a) CV comparison curves of GH and 3D cage-like Co_3O_4/NF. The asymmetric capacitor of (b) CV curves in various voltage windows at a scanning rate of 10 mV s^{-1}, (c) CV curves at various scan rates, (d) GCD curve at various potential windows at current density of 1 A g^{-1}, (e) GCD curves at different current density in the voltage window of 1.7 V, (f) Nyquist plots, (g) Ragone plot and (h) Cycling performance.

Furthermore, the slop of the line is observed to be higher than 45° in the low-frequency region, which clearly suggests that the electrochemical capacitive behavior of this asymmetric supercapacitor is not controlled by diffusion process. The ordered porosity structure in Co_3O_4/NF electrode minimized the diffusive resistance of ions, further resulting in that the asymmetric capacitor has good electrochemical performance. Figure 7h shows the cyclic performances of the asymmetric supercapacitor at the current density of 1 A g^{-1}. The capacitance retention rate is about 83% after 1500 cycles. The result indicates that the 3D cage-like Co_3O_4/NF electrode is a very potential and promising positive electrode material for asymmetric supercapacitors with high energy density and good capacitance retention.

4. CONCLUSION

In conclusion, we have synthesized the uniform and unique 3D cage-like Co_3O_4/NF electrode through a mild hydrothermal process followed by heat treatment, which is constructed by lots of aligned Co_3O_4 nanowires. It is found that the binder-free electrode possesses large volume of cage, which facilitate ion transport and an efficient and deep redox reaction, accordingly improve the utilization of Co_3O_4. Moreover, such 3D cage-like Co_3O_4 architecture directly grown on nickel foam without any conducting media and binder results in excellent supercapacitive performance in terms of the single electrode specific capacitance of 642 F g^{-1} at current density of 1 A g^{-1} with 11% loss after 1500 cycles, and the as-assembled asymmetric capacitor shows an energy density of 31 Wh kg^{-1} at power density of 854 W kg^{-1} with a wide working voltage (1.7 V).

SUPPORTING INFORMATION

1. The SEM image of different samples

For comparison, we adjust the reaction temperature and time to obtain the best comprehensive properties of $Co(OH)_2$ (heat to 100 °C and keep for 16 h denoted as CN100-16, heat up to 120°C and keep for 12h denoted as CN120-12).

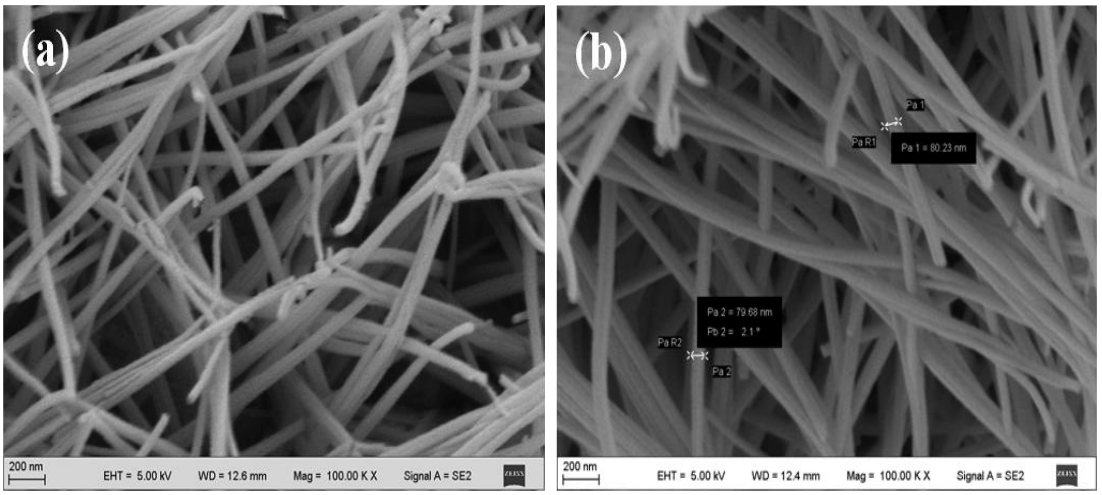

Figure S1 The SEM image of (a) CN100-16 (b) CN120-12.

As is shown in Figure S1, the nanowires with an average diameter size of about 80 nm were formed. But these nanowires still had not interwave into a cage-like architecture at the reaction temperature of 100 °C for 16 h. Similarly, when the reaction time kept for 12 h at 120 °C, they had not present the cage-like structure. Therefore, the reaction time of 16 hand temperature of 120 °C is optimal experimental condition.

2. CV curves and GCD curves of CN100-16 and CN120-12

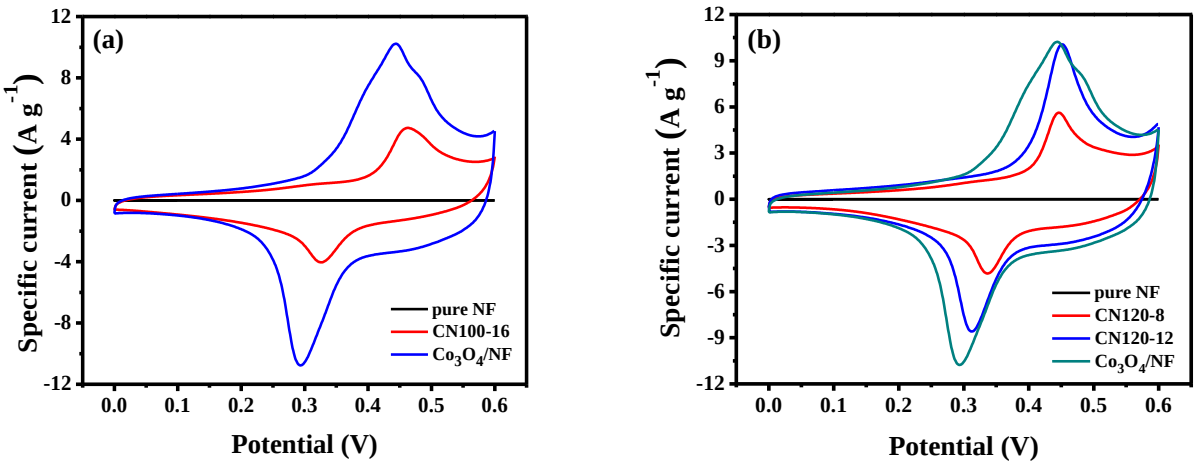

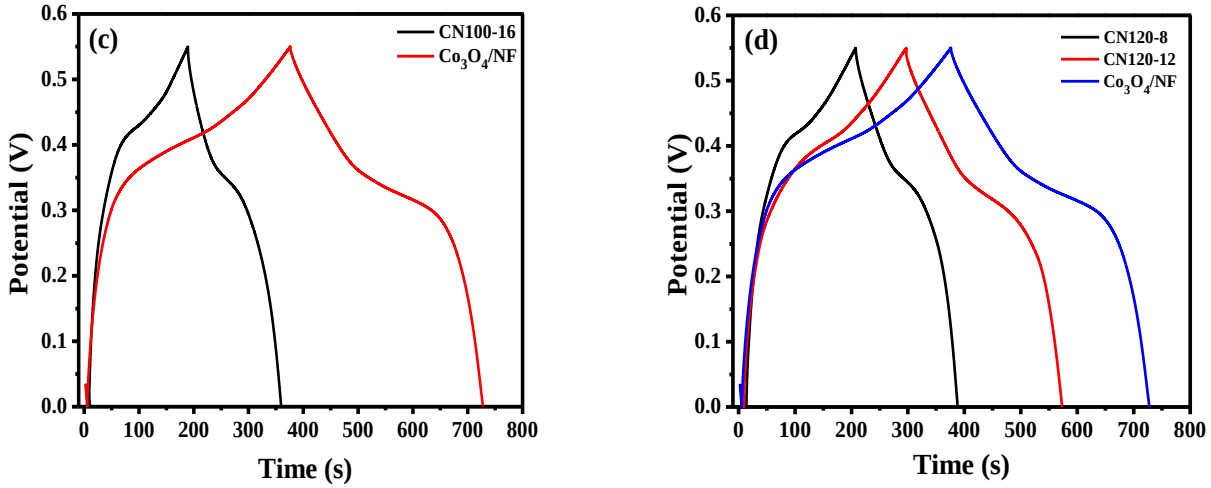

Figure S2 CV curves of (a) the pristine nickel foam, CN100-16, Co_3O_4/NF at 5 mV s^{-1}. (b) the pristine nickel foam, CN120-8, CN120-12, Co_3O_4/NF. GCD curves of (c) the CN100-16 and Co_3O_4/NF, (d) the as-prepared CN120-8, CN120-12, Co_3O_4/NF electrodes at 1 A g^{-1}.

The CV curves of the pristine nickel foam, CN100-16, Co_3O_4/NF at the same scan rate of 5mV s^{-1} are shown in Figure S2(a). It can be found that the shape of CV curves are different from the rectangular shape of an ideal capacitor as well except for nickel foam. The capacitance contribution from nickel foam substrate is so small that almost can be ignored. Co_3O_4/NF electrode is largest in the integrated CV area of three electrodes. It suggests that the Co_3O_4/NF has excellent capacitance behavior. It matches well with the result of SEM. The GCD tests are shown in Figure S2(c) and S2(d), it was run in the potential range of 0-0.55 V for different samples. The specific capacitance value of Co_3O_4/NF, CN100-16, CN120-8, CN120-12 electrode are calculated to be 642, 310, 346, 491 F g^{-1} at 1 A g^{-1}, respectively.

3. The SEM image of GH

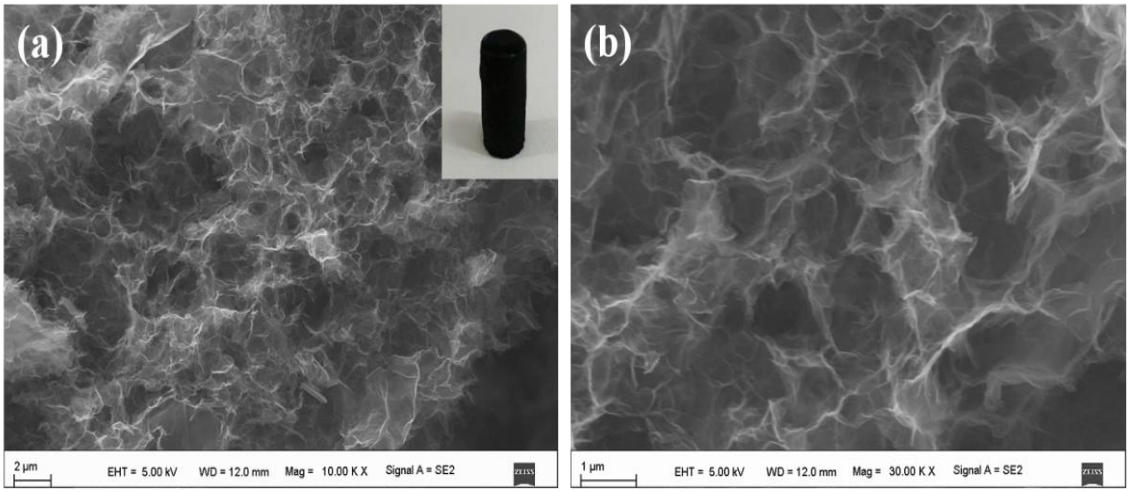

Figure S3 (a) Low-resolution (b) high-resolution of the SEM image of GH.

As is can be seen the SEM images of freeze-dried sample, GH (FigureS3a and b) possesses well-defined interconnected 3D network structure and porous structures with the wide size distribution of several micrometers formed by overlapping or stacking of the flexible graphene sheets.

ACKNOWLEDGEMENT
The author appreciates the financial supports offered by the National Natural Science Foundation of China (nos. 20963009, 21163017 and 21563027) and Specialized Research Fund for the Doctoral Program of Higher Education (no. 20126203110001).

References

1. M. Winter and R. J. Brodd, *Chem. Rev.*, 104 (2004) 4245-4270.
2. T. Y. Wei, C. H. Chen, H. C. Chien, S. Y. Lu and C. C. Hu, *Adv. Mater.*, 22 (2010) 347-351.
3. V. Subramanian, H. Zhu, R. Vajtai, Ajayan, P. M.;Wei, B. *J. Phys. Chem. B*, 109 (2005) 20207-20214.
4. J. C. Deng, L. T. Kang, G. L. Bai, Y. Li, P. Y. Li, X. G. Liu, Y. Z. Yang, F. Gao and W. Liang, *Electrochim. Acta*, 132 (2014) 127-135.
5. H. Chen, T. N. Cong, W. Yang, C. Tan, Y. Li and Y. Ding, *Prog. Nat. Sci.*, 19 (2009) 291-312.
6. L. L. Zhang and X. S. Zhao, *Chem. Soc. Rev.*, 38 (2009) 2520-2531.
7. G. A. Snook, P. Kao and A. S. Best, *J. Power Sources*, 196 (2011) 1-12.
8. M. J. Zhi, C. C. Xiang, J. T. Li, M. Li and N. Q. Wu, *Nanos cale*, 5 (2013) 72-88.
9. T. Meng, Q. Q. Xu, Z. H. Wang, Y. T. Li, Z. M. Gao, X. Y. Xing and Ren, T. Z. *Electrochim. Acta*, 180 (2015) 104-111.
10. L. B. Kong, L. Deng, J. W. Lang, X. Ji, Y. C. Luo, L. Kang, *Chin. J. Chem.*, 30 (2012) 570-576.
11. J. Xu, L. Cao, W. Wang and Z. Chen, *Electrochim. Acta*, 56 (2010) 732-736.
12. Q. Li, X. N. Hu, Q. Yang, Z. Yan, L. P. Kang, Z. B. Lei, Z. P. Yang, and Z. H. Liu, *Electrochim. Acta*, 119 (2014) 184-191.
13. F. L. Luo, J. Li, Y. Lei, W. Yang, H. Y. Yuan and D. Xiao, *Electrochim. Acta*, 135 (2014) 495-502.
14. A. G. Xiao, S. B. Zhou, C. G. Zuo, Y. B. Zhuan and X. Ding, *Mater. Res. Bull.*, 60 (2014) 674-678.
15. V. H. Nguyen, J. J. Shim, *Mater. Lett.*, 139 (2015) 377-381.
16. J. C. Liu, Y. J. Xu, X. J. Ma, J. K. Feng, Y. T. Qian and S. L. Xiong, *Nano Energy*, 7 (2014) 52-62.
17. L. C. Wu, Y. J. Chen, M. L. Mao, Q. H. Li and M. Zhang, *ACS Appl. Mater. Interfaces*, 6 (2014) 5168-5174.
18. Y. D. Zhang, Z. A. Hu, Y. R. Liang, Y. Y. Yang, N. An, Z. M. Li, H. Y. Wu, *J. Mater. Chem. A*, 3 (2015) 15057-15067.
19. N. An, Y. F. An, Z. A. Hu, B. S. Guo, Y. Y. Yang and Z. Q. Lei, *J. Mater. Chem. A*, 3 (2015) 22239-22246.
20. L. Li, Z. A. Hu, Y. Y. Yang, P. J. Liang, A. L. Lu, H. Xu, Y. Y. Hu and H. Y. Wu, *Chin. J. Chem.*, 31 (2013) 1290-1298.
21. X. J. Ma, L. B. Kong, W. B. Zhang, M. C. Liu, Y. C. Luo and L. Kang, *Electrochim. Acta*, 130 (2014) 660-669.
22. H. W. Wang, H. Yi, X. Chen and X. F. Wang, *J. Mater. Chem. A*, 2 (2014) 3223-3230.
23. J. Xu, Q. F. Wang, X. W. Wang, Q. Y. Xiang, B. Liang, D. Chen and G. Z. Shen, *ACS Appl. Mater. Interfaces*, 5 (2013) 11159-11162.
24. W. W. Liu, X. Li, M. H. Zhu and X. He, *J. Power Sources*, 282 (2015) 179-186.
25. R. B. Rakhi, W. Chen, D. Cha and H. N. Alshareef, *Nano Lett.*, 12 (2012) 2559-2567.
26. K. W. Qiu, H. L. Yan, D. Y. Zhang, Y. Lu, J. B. Cheng, W. Q. Zhao, C. L. Wang, Y. H. Zhang, X. M.

Liu, C. W. Cheng and Y. S. Luo, *Electrochim. Acta*, 141 (2014) 248-254.
27. R. Kumar, H. J. Kim, S. Park, A. Srivastava and I. K. Oh, *Carbon*, 79 (2014) 192-202.
28. Y. Y. Wang, Y. Lei, J. Li, L. Gu, H. Y. Yuan and D. Xiao, *ACS Appl. Mater. Interfaces*, 6 (2014) 6739
29. C. M. Zhang, L. J. Xie, W. Song, J. L. Wang, G. H. Sun and K. X. Li, *J. Electroanal. Chem.*, 706 (2013) 1-6.
30. Y. Q. Jiang, L. Y. Chen, H. Q. Zhang, Q. Zhang, W. F. Chen, J. K. Zhu and D. M. Song, *Chem. Eng. J.*, 292 (2016) 1-12.
31. W. Du, R. M. Liu, Y. W. Jiang, Q. Y. Lu, Y. Z. Fan and F. Gao, *J. Power Sources*, 227 (2013) 101-105.
32. S. K. Meher and G. R. Rao, *J. Phys. Chem. C*, 115 (2011) 15646-15654.
33. S. B. Ye, J. C. Feng and P. Y. Wu, *ACS Appl. Mater. Interfaces*, 5 (2013) 7122-7129.
34. X. H. Xiong, D. Ding, D. C. Chen, G. Waller, Y. F. Bu, Z. X. Wang and M. L. Liu, *Nano Energy*, 11 (2015) 154-161.
35. S. K. Ujjain, G. Singh and R. K. Sharma, *Electrochim. Acta*, 169 (2015) 276-282.
36. H. G. Wei, C. Z. He, J. R. Liu, H. B. Gu, Y. R. Wang, X. R. Yan, J. Guo, D. W. Ding, N. Z. Shen, X. F. Wang, S.Y. Wei and Z. H. Guo, *Polymer*, 67 (2015) 192-199.
37. P. Yuan, N. Zhang, D. Zhang, T. Liu, L. M. Chen, X. H. Liu, R. Z. Ma and G. Z. Qiu, *Chem. Commun.*, 50 (2014) 11188-11191.
38. X. Tan, H. Y. Gao, M. Yang, Y. Luan, W. J. Dong, Z. K. Jin, J. Yu, Y. Qi, Y. H. Fen and G. Wang, *J. Alloys Comp.*, 608 (2014) 278-282.
39. K. W. Qiu, Y. Lu, J. B. Cheng, H. L. Yan, X. Y. Hou, D. Y. Zhang, M. Lu, X. M. Liu and Y. S. Luo, *Electrochim. Acta*, 157 (2015) 62-68.
40. J. Zhang, J. P. Cheng, M. Li, L. Liu, F. Liu and X. B. Zhang, *J. Electroanal. Chem.*, 743 (2015) 38-45.
41. Q. Q. Ke, C. H. Tang, Z. C. Yang, M. R. Zheng, L. Mao, H. J. Liu and J. Wang, *Electrochim. Acta*, 163 (2015) 9-15.
42. J. B. Wu, Y. Lin, X. H. Xia, J. Y. Xu and Q. Y. Shi, *Electrochim. Acta*, 56 (2011) 7163-7170.
43. X. H. Xia, J. P. Tu, Y. Q. Zhang, Y. J. Mai, X. L. Zhang, C. D. Gu and X. B. Zhao, *J. Mater. Chem.*, 11 (2011) 9319-9325.
44. U. M. Patil, J. S. Sohn, S. B. Kulkarni, S. C. Lee, H. G. Park, K. V. Gurav, J. H. Kim and S. C. Jun, *ACS Appl. Mater. Interfaces*, 6 (2014) 2450-2458.
45. K. Deori, S. K. Ujjain, R. K. Sharma and S. Deka, *ACS Appl. Mater. Interfaces*, 5 (2013) 10665-10672.